SUPPLEMENTARY INFORMATION

## Appendix A: Effect of the WPA on characterization of electron wavepacket

We reconstructed the $S_{SFA}$ shown in Figure 2 (a) using the VTGPA which requires the application of the WPA due to the fact that the DTME is not known apriori. The retrieved dipole phase and the corresponding GD are shown by the blue curves in Figure S 1 (a) and (b), respectively. The deviation from the theory curve (black lines) used to simulate the $S_{SFA}$ shows the effect introduced by the WPA when trying to reconstruct the electron wavepacket using conventional algorithms. In general, the WPA leads to a smoothing of the retrieved phase profile as a function of energy. Similar errors are reported in [1].

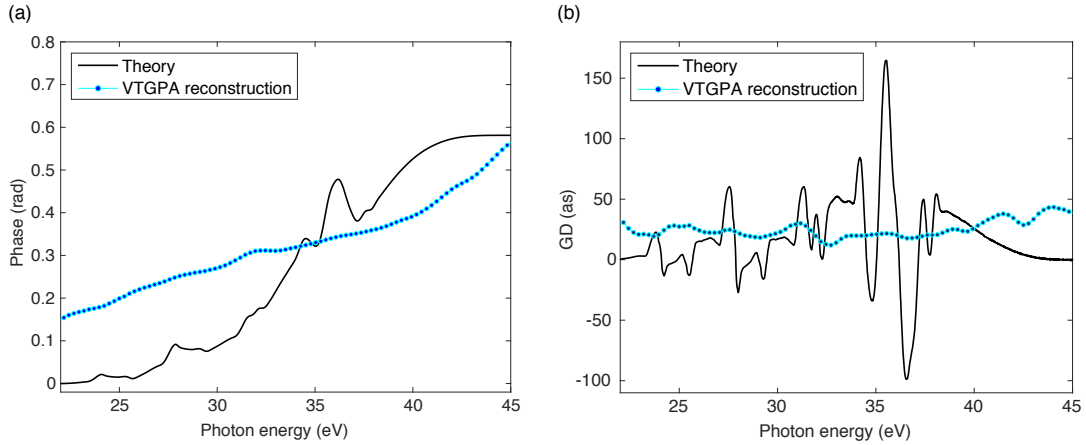


**Figure S 1.** Retrieved (a) phase and (b) GD using the VTGPA algorithm for the $S_{SFA}$ shown in Figure 2. The black curves represent the theory curves for the phase and GD used to simulate $S_{SFA}$.

## Appendix B: Full derivation of the ACDC algorithm

Continuing from section 4 we present here the full derivation of $\tilde{d}$. We can write the full expression of $M$ from equation (14) using the expression of $\tilde{a}[l,m]$ (equation (12)). This results in:

$$\begin{aligned} M = \sum_l \sum_m & d[m]^2 \Gamma[l,m]^2 + \frac{d[m+1]^2 \beta[l,m]^2}{\Delta k[m]^2} + \frac{d[m-1]^2 \beta[l,m]^2}{\Delta k[m]^2} + a[l,m]^2 \\ & + 2\Re\left( \tilde{d}[m]\tilde{\Gamma}[l,m] \frac{\tilde{d}[m+1]^* \tilde{\beta}[l,m]^*}{\Delta k[m]} - \tilde{d}[m]\tilde{\Gamma}[l,m] \frac{\tilde{d}[m-1]^* \tilde{\beta}[l,m]^*}{\Delta k[m]} \right. \\ & - \tilde{d}[m]\tilde{\Gamma}[l,m]\tilde{a}'[l,m]^* - \frac{\tilde{d}[m+1]\tilde{d}[m-1]^* \beta[l,m]^2}{\Delta k[m]^2} - \frac{\tilde{d}[m+1]\tilde{\beta}[l,m]\tilde{a}'[l,m]^*}{\Delta k[m]} \\ & \left. + \frac{\tilde{d}[m-1]\tilde{\beta}[l,m]\tilde{a}'[l,m]^*}{\Delta k[m]} \right) \end{aligned} \quad \text{(S 1)}$$

We consider the derivative of this expression with respect to the term $m = c$. The only terms of $M$ that matter are $M_c$, $M_{c+1}$ and $M_{c-1}$. These terms are defined in the following equations

$$
\begin{aligned}
M_c \;=& \sum_l d[c]^2\Gamma[l,c]^2 + \frac{d[c+1]^2\beta[l,c]^2}{\Delta k[c]^2} + \frac{d[c-1]^2\beta[l,c]^2}{\Delta k[c]^2} + a[l,c]^2 \\
&+ 2\Re\left(\tilde{d}[c]\tilde{\Gamma}[l,c]\frac{\tilde{d}[c+1]^*\tilde{\beta}[l,c]^*}{\Delta k[c]} - \tilde{d}[c]\tilde{\Gamma}[l,c]\frac{\tilde{d}[c-1]^*\tilde{\beta}[l,c]^*}{\Delta k[c]}\right. \\
&- \tilde{d}[c]\tilde{\Gamma}[l,c]\tilde{a}'[l,c]^* - \frac{\tilde{d}[c+1]\tilde{d}[c-1]^*\beta[l,c]^2}{\Delta k[c]^2} - \frac{\tilde{d}[c+1]\tilde{\beta}[l,c]\tilde{a}'[l,c]^*}{\Delta k[c]} \\
&\left.+ \frac{\tilde{d}[c-1]\tilde{\beta}[l,c]\tilde{a}'[l,c]^*}{\Delta k[c]}\right)
\end{aligned}
\tag{S 2}
$$

$$
\begin{aligned}
M_{c+1} \;=& \sum_l d[c+1]^2\Gamma[l,c+1]^2 + \frac{d[c+2]^2\beta[l,c+1]^2}{\Delta k[c+1]^2} + \frac{d[c]^2\beta[l,c+1]^2}{\Delta k[c+1]^2} + a[l,c+1]^2 \\
&+ 2\Re\left(\tilde{d}[c+1]\tilde{\Gamma}[l,c+1]\frac{\tilde{d}[c+2]^*\tilde{\beta}[l,c+1]^*}{\Delta k[c+1]}\right. \\
&- \tilde{d}[c+1]\tilde{\Gamma}[l,c+1]\frac{\tilde{d}[c]^*\tilde{\beta}[l,c+1]^*}{\Delta k[c+1]} - \tilde{d}[c+1]\tilde{\Gamma}[l,c+1]\tilde{a}'[l,c+1]^* \\
&- \frac{\tilde{d}[c+2]\tilde{d}[c]^*\beta[l,c+1]^2}{\Delta k[c+1]^2} - \frac{\tilde{d}[c+2]\tilde{\beta}[l,c+1]\tilde{a}'[l,c+1]^*}{\Delta k[c+1]} \\
&\left.+ \frac{\tilde{d}[c]\tilde{\beta}[l,c+1]\tilde{a}'[l,c+1]^*}{\Delta k[c+1]}\right)
\end{aligned}
\tag{S 3}
$$

$$
\begin{aligned}
M_{c-1} \;=& \sum_l d[c-1]^2\Gamma[l,c-1]^2 + \frac{d[c]^2\beta[l,c-1]^2}{\Delta k[c-1]^2} + \frac{d[c-2]^2\beta[l,c-1]^2}{\Delta k[c-1]^2} + a[l,c-1]^2 \\
&+ 2\Re\left(\tilde{d}[c-1]\tilde{\Gamma}[l,c-1]\frac{\tilde{d}[c]^*\tilde{\beta}[l,c-1]^*}{\Delta k[c-1]}\right. \\
&- \tilde{d}[c-1]\tilde{\Gamma}[l,c-1]\frac{\tilde{d}[c-2]^*\tilde{\beta}[l,c-1]^*}{\Delta k[c-1]} - \tilde{d}[c-1]\tilde{\Gamma}[l,c-1]\tilde{a}'[l,c-1]^* \\
&- \frac{\tilde{d}[c]\tilde{d}[c-2]^*\beta[l,c-1]^2}{\Delta k[c-1]^2} - \frac{\tilde{d}[c]\tilde{\beta}[l,c-1]\tilde{a}'[l,c-1]^*}{\Delta k[c-1]} \\
&\left.+ \frac{\tilde{d}[c-2]\tilde{\beta}[l,c-1]\tilde{a}'[l,c-1]^*}{\Delta k[c-1]}\right)
\end{aligned}
\tag{S 4}
$$

From these expressions we need to solve the system of equations (15). If we consider the derivative respect to the magnitude $d[c]$ of the complex DTME we obtain:

$$
\begin{aligned}
\frac{\partial M_c}{\partial d[c]} \;=& \sum_l 2d[c]\Gamma[l,c]^2 \\
&+ 2\Re\left(e^{i\phi[c]}\tilde{\Gamma}[l,c]\frac{\tilde{d}[c+1]^*\tilde{\beta}[l,c]^*}{\Delta k[c]} - e^{i\phi[c]}\tilde{\Gamma}[l,c]\frac{\tilde{d}[c-1]^*\tilde{\beta}[l,c]^*}{\Delta k[c]}\right. \\
&\left.- e^{i\phi[c]}\tilde{\Gamma}[l,c]\tilde{a}'[l,c]^*\right)
\end{aligned}
\tag{S 5}
$$

 

$$\frac{\partial M_{c+1}}{\partial d[c]} = \sum_l \frac{2d[c]\beta[l,c+1]^2}{\Delta k[c+1]^2} + 2\Re\left(-e^{i\phi[c]}\tilde{d}[c+1]^*\tilde{\Gamma}[l,c+1]^*\frac{\tilde{\beta}[l,c+1]}{\Delta k[c+1]} - e^{i\phi[c]}\frac{\tilde{d}[c+2]\beta[l,c+1]^2}{\Delta k[c+1]^2} + e^{i\phi[c]}\frac{\tilde{\beta}[l,c+1]\tilde{a}'[l,c+1]^*}{\Delta k[c+1]}\right) \quad \text{(S 6)}$$

$$\frac{\partial M_{c-1}}{\partial d[c]} = \sum_l \frac{2d[c]\beta[l,c-1]^2}{\Delta k[c-1]^2} + 2\Re\left(e^{i\phi[c]}\tilde{d}[c-1]^*\tilde{\Gamma}[l,c-1]^*\frac{\tilde{\beta}[l,c-1]}{\Delta k[c-1]} - e^{i\phi[c]}\frac{\tilde{d}[c-2]^*\beta[l,c-1]^2}{\Delta k[c-1]^2} - e^{i\phi[c]}\frac{\tilde{\beta}[l,c-1]\tilde{a}'[l,c-1]^*}{\Delta k[c-1]}\right) \quad \text{(S 7)}$$

If we now introduce the following expressions:

$$\tilde{\delta}[l,c] = \tilde{\Gamma}[l,c]\frac{\tilde{d}[c+1]^*\tilde{\beta}[l,c]^*}{\Delta k[c]} - \tilde{\Gamma}[l,c]\frac{\tilde{d}[c-1]^*\tilde{\beta}[l,c]^*}{\Delta k[c]} - \tilde{\Gamma}[l,c]\tilde{a}'[l,c]^* \quad \text{(S 8)}$$

$$\tilde{\eta}[l,c] = -\tilde{d}[c+1]^*\tilde{\Gamma}[l,c+1]^*\frac{\tilde{\beta}[l,c+1]}{\Delta k[c+1]} - \frac{\tilde{d}[c+2]\beta[l,c+1]^2}{\Delta k[c+1]^2} + \frac{\tilde{\beta}[l,c+1]\tilde{a}'[l,c+1]^*}{\Delta k[c+1]} \quad \text{(S 9)}$$

$$\tilde{\gamma}[l,c] = \tilde{d}[c-1]^*\tilde{\Gamma}[l,c-1]^*\frac{\tilde{\beta}[l,c-1]}{\Delta k[c-1]} - \frac{\tilde{d}[c-2]^*\beta[l,c-1]^2}{\Delta k[c-1]^2} - \frac{\tilde{\beta}[l,c-1]\tilde{a}'[l,c-1]^*}{\Delta k[c-1]} \quad \text{(S 10)}$$

Using these expressions, we can write a simplified formula for $\frac{\partial M}{\partial d[c]}$ which reads

$$\frac{\partial M}{\partial d[c]} = \sum_l 2d[c]\Gamma[l,c]^2 + \frac{2d[c]\beta[l,c+1]^2}{\Delta k[c+1]^2} + \frac{2d[c]\beta[l,c-1]^2}{\Delta k[c-1]^2} + 2\Re\left(e^{i\phi[c]}\left(\tilde{\gamma}[l,c] + \tilde{\delta}[l,c] + \tilde{\eta}[l,c]\right)\right) \quad \text{(S 11)}$$

With the same idea we can find the expression of $\frac{\partial M}{\partial \phi[c]}$ which results in

$$\frac{\partial M}{\partial \phi[c]} = \sum_l 2\Re\left(id[c]e^{i\phi[c]}\left(\tilde{\gamma}[l,c] + \tilde{\delta}[l,c] + \tilde{\eta}[l,c]\right)\right) \quad \text{(S 12)}$$

that can be rewritten in the following way

 

$$\frac{\partial M}{\partial \phi[c]} = \sum_{l} -2d[c]\Im\left(e^{i\phi[c]}\left(\tilde{\gamma}[l,c] + \tilde{\delta}[l,c] + \tilde{\eta}[l,c]\right)\right) \tag{S 13}$$

To solve the system of equations (15) we set both the equations (S 11) and (S 13) equal to zero. After some manipulation one get

$$\begin{aligned} 0 = \sum_{l} 2d[c]\Gamma[l,c]^2 + \frac{2d[c]\beta[l,c+1]^2}{\Delta k[c+1]^2} + \frac{2d[c]\beta[l,c-1]^2}{\Delta k[c-1]^2} \\ + 2\Re\left(e^{i\phi[c]}\left(\tilde{\gamma}[l,c] + \tilde{\delta}[l,c] + \tilde{\eta}[l,c]\right)\right) + 2i\Im\left(e^{i\phi[c]}\left(\tilde{\gamma}[l,c] + \tilde{\delta}[l,c] + \tilde{\eta}[l,c]\right)\right) \end{aligned} \tag{S 14}$$

The real and imaginary part are the same, so we can just break it out and rewrite (S 14) as

$$0 = \sum_{l} 2d[c]\Gamma[l,c]^2 + \frac{2d[c]\beta[l,c+1]^2}{\Delta k[c+1]^2} + \frac{2d[c]\beta[l,c-1]^2}{\Delta k[c-1]^2} + 2e^{i\phi[c]}\left(\tilde{\gamma}[l,c] + \tilde{\delta}[l,c] + \tilde{\eta}[l,c]\right) \tag{S 15}$$

We can finally solve for $\tilde{d}[n] = d[n]e^{i\phi[n]}$ which results in the final expression

$$\tilde{d}[c] = \frac{-\left(\sum_l \tilde{\gamma}[l,c]^* + \tilde{\delta}[l,c]^* + \tilde{\eta}[l,c]^*\right)}{\sum_l \Gamma[l,c]^2 + \frac{\beta[l,c+1]^2}{\Delta k[c+1]^2} + \frac{\beta[l,c-1]^2}{\Delta k[c-1]^2}} \tag{S 16}$$

The output result is then refined by using a stochastic gradient descent algorithm. Starting from the complex DTME $\tilde{d}$ solved by the ACDC algorithm, we use the gradient descent algorithm to further minimize the figure of merit. First, the gradient descent algorithm adds an arbitrarily small quantity $\Delta\phi$ to the $m^{\text{th}}$ energy point of the DTME phase

$$\phi_{\text{in}}[m] = \phi_{\text{in}}[m] + \Delta\phi. \tag{S 17}$$

The error associated to the spectrogram generated by the updated DTME function ($\varepsilon_{\text{new}}$) is compared with the starting error ($\varepsilon_{\text{start}}$). This provides an estimation of the gradient of the error function $\mathcal{E}$ that we want to minimize

$$\nabla\mathcal{E} = \frac{\varepsilon_{\text{new}} - \varepsilon_{\text{start}}}{\Delta\phi}. \tag{S 18}$$

From this we assign the new DTME phase value at the energy point $m$

$$\phi_{\text{out}}[m] = \phi_{\text{in}}[m] - \eta\nabla\mathcal{E} \tag{S 19}$$

where $\eta$ is the so-called learning rate. The same procedure is applied to the amplitude terms of the DTME vector and one iteration loop is completed when both amplitude and phase have been updated at each energy point. For the phase points we combined the gradient descent algorithm with Adam optimizer which modifies the value of $\nabla\mathcal{E}$ which is used in equation (S 19) resulting in a faster converging process. The details of the Adam optimizer can be found in the reference [24].

The reason why we apply a refinement of the complex $\tilde{d}$ using the stochastic gradient descent algorithm comes from the fact that in the mathematical derivation of $\tilde{d}$ a Taylor expansion up to the first order (equation (7)) has been used. This is a valid approximation as long as $\tilde{d}$ remains linear in the range $(k + \min(A)) \leq k \leq$

 

$(k + \max(A))$. In this approximation the intensity $I_0$ of the streaking field which determines the amplitude of the vector potential $A$ plays a significant role.

In Figure S 2 (a) we show the retrieved GD just using the equation (S 16) from simulated spectrograms characterized by three different IR intensities: $1\times10^{10}$ W/cm$^2$ (red symbols), $5\times10^{10}$ W/cm$^2$ (blue symbols) and $1\times10^{11}$ W/cm$^2$ (green symbols). For all the three spectrograms the same XUV pulse has been considered characterized by a spectral intensity centred at 32.5 eV, a chirp of -0.025 fs2 and FWHM bandwidth of ~5.5 eV. The fast oscillations of the theory curve (black line from reference [3]) are perfectly retrieved in the lowest IR intensity case. For $I_0$ of $5\times10^{10}$ W/cm$^2$ and $1\times10^{11}$ W/cm$^2$ a smoothening in the retrieved GD compared to the input curve is visible even though the qualitative trend is reproduced. The observed smoothening effect as $I_0$ increases is related to the truncation of the Taylor expansion of the complex DTME at the first order as $\tilde{d}$ is no longer linear over the range $(k + \min(A)) \leq k \leq (k + \max(A))$ for all $k$.

When we refine the result from equation (S 16) using a stochastic gradient descent algorithm we can overcome this limitation on the intensity $I_0$ of the IR field. We tested the result using the additional step with the gradient descent algorithm for three different IR intensities: $1\times10^{11}$ W/cm$^2$, $1\times10^{12}$ W/cm$^2$ and $1\times10^{13}$ W/cm$^2$. The results are shown in Figure S 2 (b) and are represented by the red, blue and green symbols, respectively. We observe a good agreement with the theoretical curve (black line) for all the IR intensities used to simulate the spectrograms. Note that for this specific analysis, the theoretical input curve (black line) has been extended at energies below 27.8 eV and above 40.5 eV in order to be able to simulate the spectrograms avoiding unphysical abrupt jumps in the simulated spectrogram amplitude (see black dashed line in Figure S 2).

The first step (up to equation (S 16)) of the algorithm is computationally inexpensive compared to the optimization step with the stochastic gradient descent algorithm. For this reason, running few iterations (1000 iterations) with the ACDC algorithm before considering the gradient descent algorithm improves the convergence process, reaching a lower final error when compared to the gradient descent algorithm only.

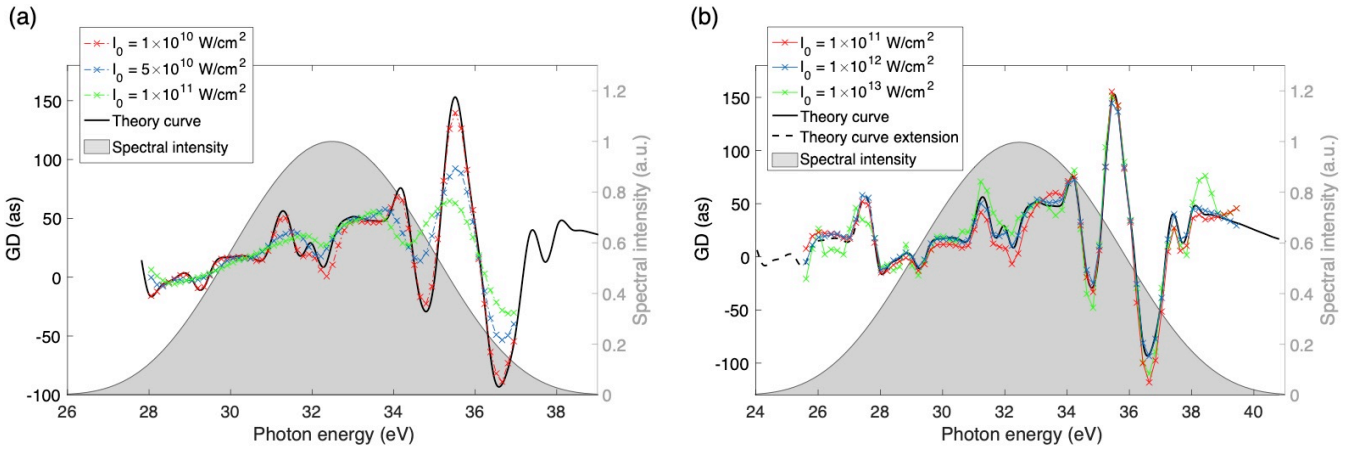


**Figure S 2.** (a) Retrieved GD using the ACDC algorithm up to the equation (S 16) for IR intensities of $1\times10^{10}$ W/cm$^2$ (red symbols), $5\times10^{10}$ W/cm$^2$ (blue symbols) and $1\times10^{11}$ W/cm$^2$ (green symbols). (b) Retrieved GD using the additional optimization step with stochastic gradient descent algorithm for IR intensities of $1\times10^{11}$ W/cm$^2$ (red symbols), $1\times10^{12}$ W/cm$^2$ (blue symbols) and $1\times10^{13}$ W/cm$^2$ (green symbols).

### Appendix C: Validation of the ACDC algorithm upon different streaking parameters

In appendix A we demonstrated the ability of the ACDC algorithm to retrieve fast GD oscillations within few eV for different IR intensities. Here we want to test the reliability of the ACDC algorithm reconstructions for different XUV bandwidths and chirp values.

In Figure S 3 (a) we plot the results for XUV with FWHM bandwidths of ~3.8 eV (red line and red shaded area) and ~10.7 eV (blue line). We plotted for completeness also the green line representing the result for the FWHM bandwidth of ~7.4 eV already reported in Figure S 2 (b). We considered for this analysis a constant IR peak intensity

 

of $1\times10^{12}$ W/cm$^2$ and XUV chirp of -0.025 fs$^2$. The features of the theory curve (black line) are perfectly resolved regardless of the XUV bandwidth considered.

In the same fashion, we tested the robustness of the retrieval algorithms to the XUV chirp. In Figure S 3 (b) we plot the retrieved GDs using values of XUV chirp: 0 fs$^2$ (red symbols), -0.015 fs$^2$ (blue symbols) and -0.025 fs$^2$ (green symbols). To simulate the spectrograms, we choose an XUV spectrum with FWHM bandwidth of ~7.4 eV (grey shaded area) and $I_0 = 1\times10^{12}$ W/cm$^2$. For chirped pulses and for the transform limited XUV pulse the retrieved GD reproduces accurately the theory curve (black line) making the two algorithms robust to different XUV chirp values. We found in general that phase changes near the central energy of the XUV pulse are more difficult to retrieve. For the transform-limited pulse, we observe a deviation of the retrieved GD from the theoretical curve of few points around the central energy of the XUV spectral intensity. Interestingly, we found that for the case of transform-limited pulses the solution is in fact not defined just at the central energy, while for the chirped pulses no significant error was observed.

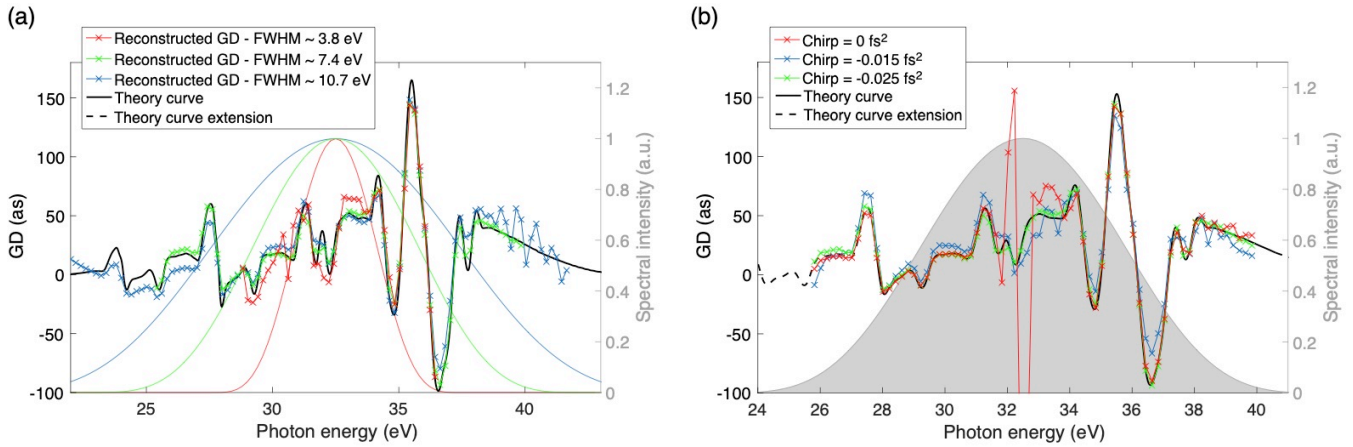


**Figure S 3.** (a) Red, green and blue symbols show the retrieved GD using the ACDC algorithm for XUV pulses centred at 32.5 eV, chirp of -0.025 fs$^2$ and FWHM bandwidths of ~3.8 eV (red line), ~7.4 eV (green line) and ~ 10.7 eV (blue line). (b) Retrieved GD using the ACDC algorithm for different XUV chirp values: 0 fs$^2$ (red symbols), -0.015 fs$^2$ (blue symbols) and -0.025 fs$^2$ (green symbols). The XUV spectral intensity is shown with the grey shaded area and is centred at 32.5 eV with FWHM bandwidth of ~ 7.4 eV. The IR field is kept constant for the three simulated spectrograms with an intensity of $1\times10^{12}$ W/cm$^2$.

## Appendix D: Noise analysis

Experimental measurements will always present a certain level of noise. Thus, testing the robustness of the combined algorithms against noise is important. It is worth highlighting the fact that, since the GD requires a differentiation of the retrieved dipole phase (see equation 2), so any noise-fluctuation will be amplified making the entire analysis challenging.

We define the signal-to-noise ratio (SNR) in the following way

$$\mathrm{SNR} = \frac{\sqrt{\sum_{l,m} P[l,m]^2}}{\sqrt{\sum_{l,m} N[l,m]^2}} \qquad \text{(S 20)}$$

where $N[l,m]$ is the Poisson noise amplitude at the position of the $l$-time pixel and $m$-energy pixel.

Since we want to reconstruct experimental measurements, we considered the XUV and the IR field parameters similar to the experimental conditions. In particular, we considered both the XUV spectrum (see grey shaded area in Figure S 4) and IR streaking field ($I_0 = 3\times10^{12}$ W/cm$^2$) close to the experimental conditions.

In Figure S 4, the red line represents the reconstructed GD using the ACDC algorithm considering only a window of 2 fs in the pump-probe delay of the spectrogram for the noise free case. Such pump-probe delay window is enough to retrieve the GD information in the absence of noise. Adding artificial Poisson noise to the spectrogram,

 

however, leads to a loss of information. An efficient way to recover such information is to reconstruct different pump-probe delay windows and average the output GD curves. In this way, the random noise contributions are averaged out while the GD information remains unaffected. To test this procedure, we added an amount of noise to the simulated spectrogram corresponding to a SNR level of ∼7 according to equation (S 20). We reconstruct the obtained spectrogram after subdividing it in 19 different pump-probe delay windows, each having a width of 2 fs. Another approach would be to reduce the number of trace portions while broadening the pump-probe delay window. Assuming that the noise level is constant over the pump-probe delay scan, broadening the pump-probe delay window that we consider for the reconstruction will increase the normalized amount information with respect to the noise level that we provide to the algorithm. We confirmed this fact considering pump-probe delay of 6 fs of the noisy spectrogram and averaging 12 reconstructions. We could achieve the same qualitatively good result which is shown in Figure S 4. The SNR value of ∼7 was chosen based on the estimated noise levels observed in our experimental data.

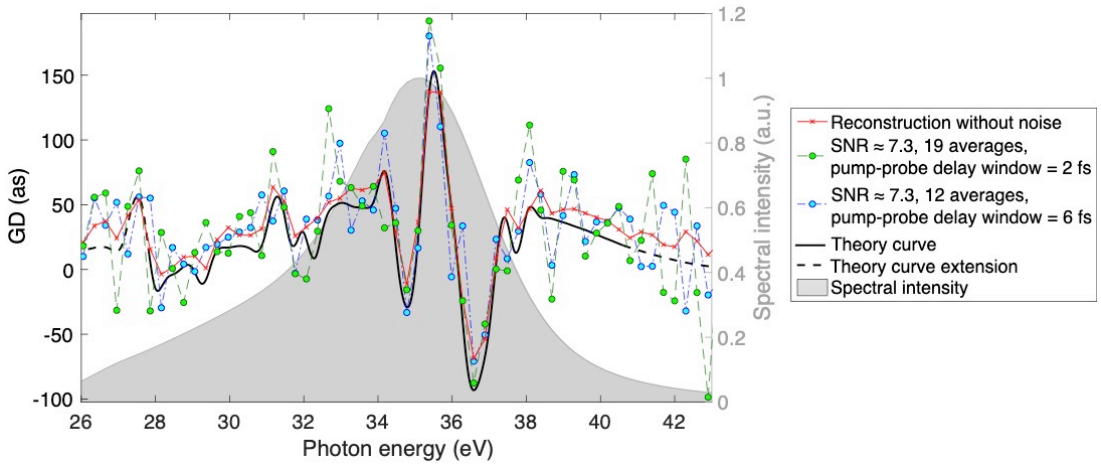


**Figure S 4.** Weighted average of 19 reconstructions on different pump probe delay windows of 2 fs of the noisy trace (green symbols) together with the weighted average of 12 reconstructions on different pump probe delay windows of 6 fs of the noisy trace (blue symbols). The theory curve used as input to generate the simulated spectrogram is shown by the black line.

In order to estimate the noise level that better approximate the experimental measurement we considered three noise levels which correspond to a SNR (defined by equation (S 20)) of approximately 23, 7.3 and 2.2. The original spectrogram together with those affected by the three noise levels are shown in Figure S 5.

In order to evaluate the SNR in the experimental measurement, we considered the photoemitted electron counts at each pump-probe delay bin in the Ne spectrogram. In Figure S 6(a) we plot with the blue line the photoemitted electron counts for the first delay bin. To isolate the signal, we applied a filtering procedure in the Fourier space where we eliminate the high noise components (see Figure S 6(b)). After filtering, the photoelectron count distribution results in the red line shown in Figure S 6(a). This photoelectron distribution gives an estimation of the signal level in our measurement which is then compared with the measured blue photoelectron distribution. Using

 

this approach, we computed the SNR estimation of the experimental measurement performing the described filtering procedure for each pump-probe delay bins and averaging the SNR values obtained over all the delay steps.

This approach has been used to estimate the SNRs for the noisy simulated spectrograms shown in Figure S 5(b), (c) and (d). The resulting SNR values are 36, 12 and 4.4 respectively. In all the three cases the evaluated SNR with

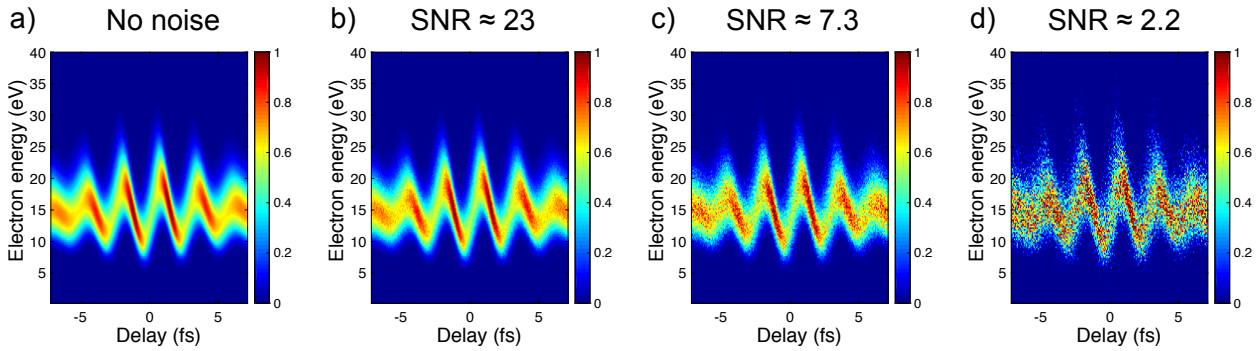


**Figure S 5.** (a) Simulated streaking spectrogram considered for testing the ACDC algorithm upon added Poisson noise. Three different noise levels have been considered and compared to the experimental case producing the spectrograms shown in (b) (SNR ≈ 23), (c) (SNR ≈ 7.3) and (d) (SNR ≈ 2.2).

the described filtering procedure is overestimated if compared with the ones computed with equation (S 20) which leads to the values of 23, 7.3 and 2.2 respectively. However, the respective ratios are kept approximately the same.

Computing the SNR using the method described in this section on the experimental spectrogram we obtain the values of 13 and 11.7 for Ar and Ne, respectively. This brought us to assert that the SNR level in the experimental conditions analysed in this work can approximately be compared with SNR of about 7.3.

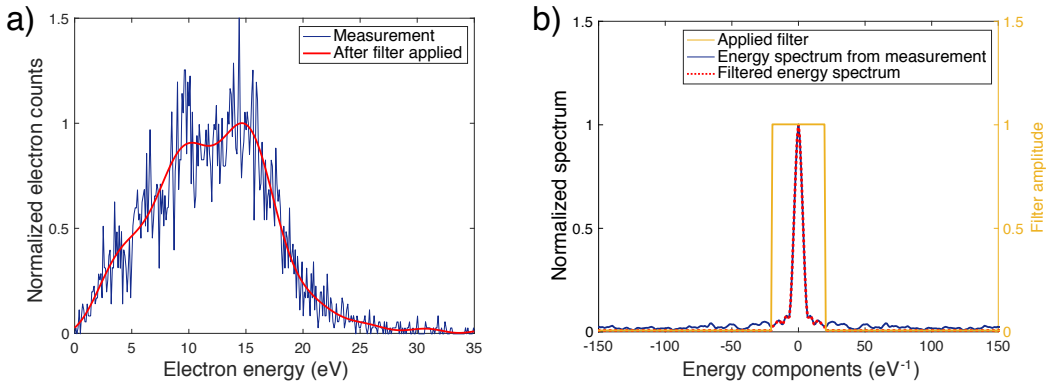


**Figure S 6.** Photoelectron counts distribution (blue line) normalized with respect to the filtered distribution (red line) corresponding to the first pump-probe delay step of the experimental Ne spectrogram. The energy components in the Fourier space of the measured photoelectron distribution are shown in (b) by the blue line. The red dotted line represents the portion of spectrum considered after the filter (yellow line) has been applied and which results in the red line in (a).

## Appendix E: Procedure for retrieving the dipole phase from experimental measurement using the ACDC algorithm

In section 5 we reported the dipole phase of Ar (Figure 4) reconstructed from the experimental streaking measurement shown in Figure 1 using the ACDC algorithm together with the computed GD difference between Ar and Ne (Figure 5). Here we describe in detail all the steps we followed to obtain the final result using the ACDC algorithm.

 

The first step consists in the characterization of both the XUV and IR fields. For this purpose, we considered the Ne spectrogram as a reference. We reconstructed, using VTGPA, three different pump-probe delay windows of 3 fs each (3-7 fs, 6-9 fs and 8.5-11.5 fs) of the Ne spectrogram, corresponding to the main oscillations in the streaking spectrogram. With the VTGPA we included the DTME of Ne in the reconstruction and extracted the information about the XUV and IR fields. We iterate for 3000 iterations and we considered the $\tilde{d}$ of Ne from reference [25].

To increase the accuracy of the streaking field reconstruction, an additional refinement only on the IR field has been performed after the 3000 iterations considering a wider pump probe delay window of 5 fs cantered around the original 3 fs pump probe delay window.

Since the Ar and Ne streaking spectrograms have been measured under the same experimental conditions thanks to the coincidence detection of the COLTRIMS apparatus we can assume that the XUV and IR fields characterized using the Ne spectrograms apply as well for Ar.

The characterized XUV and IR fields become then the inputs for the ACDC algorithm where now the target is the Ar spectrogram. Keeping fixed the XUV and IR fields characterized using VTGPA from the first pump-probe delay window (3-7 fs) of the Ne spectrogram, we selected 12 pump-probe delay windows of 2.5 fs (2.6-5.1 fs, 2.8-5.3 fs, 3.0-5.5 fs, 3.2-5.7 fs, 3.4-5.9 fs, 3.6-6.1 fs, 3.8-6.3 fs, 4-6.5 fs, 4.2-6.7 fs, 4.4-6.9 fs, 4.6-7.1 fs and 4.8-7.3 fs), around the 3-7 fs pump-probe delay window, for the Ar spectrogram which have been reconstructed by the ACDC algorithm. This procedure has been repeated similarly for the other two pump-probe delay windows used in the characterization step with the Ne spectrogram (6-9 fs and 8.5-11.5 fs) resulting in 36 total reconstructions using the ACDC algorithm. We considered 1000 iterations using the ACDC algorithm up to equation (S 16) as described in appendix A followed by 5000 iterations using the gradient descent algorithm described in appendix A. The final 36 reconstructions have been weighted averaged and resulted in the final dipole phase of Ar with its corresponding standard deviation shown in Figure 4.

## Appendix F: Acronyms

| | |
|---|---|
| ACDC | absolute complex dipole transition matrix element reconstruction |
| APT | attosecond pulse train |
| COLTRIMS | Cold target recoil ion momentum spectrometer [18] |
| DTME | dipole transition matrix element |
| FROG-CRAB | frequency resolved optical gating for complete retrieval of attosecond burst [21], [22] |
| GD | group delay |
| IR | infrared |
| RABBITT | reconstruction of attosecond beating by interference of two-photon transition [8], [9] |
| SAP | single attosecond pulse |
| SFA | strong-field approximation |
| VTGPA | Volkov transform generalized projections algorithm [23] |
| XUV | extreme ultraviolet |

**Table 1.** List of the main acronyms used throughout this paper.

 